International Journal of Solids and Structures 238 (2022) 111379

Contents lists available at ScienceDirect

International Journal of Solids and Structures

journal homepage: www.elsevier.com/locate/ijsolstr

3D zero-thickness interface model for fracture of cement-based materials with chemical degradation

Ariadna Martínez [a], Joaquín Liaudat [b,*], Carlos M. López [a], Ignacio Carol [a]

[a] Department of Civil and Environmental Engineering, Universitat Politècnica de Catalunya, 08034 Barcelona, Spain
[b] Faculty of Civil Engineering and Geosciences, Delft University of Technology, 2628 CN Delft, The Netherlands

ARTICLE INFO

Keywords:
Interface elements
Constitutive law
Fracture mechanics
Geomaterials
Chemical degradation

ABSTRACT

In the framework of the Finite Element Method, zero-thickness interface elements have been widely used to model fracturing processes in quasi-brittle materials in a broad variety of problems. In particular, interface elements equipped with elastoplastic constitutive laws that account for the softening of the material strength parameters due to the fracturing mechanical work has been proved to accurately reproduce observed fracture propagation behaviour in concrete. Along this line, this paper presents the extension of an existing constitutive law of this kind to include the effect of chemical degradation of the material in the formation of fractures. The law is defined in terms of the normal and shear stresses on the average plane of the crack and the corresponding normal and shear relative displacements. A hyperbolic cracking (plastification) surface in the stress state determines the crack initiation. The softening of the cracking surface is governed by two history variables: an internal variable that accounts for the dissipated fracturing (plastic) work, and an external variable to be provided by a chemical degradation model that accounts for the effect of chemical degradation on the strength parameters. After a detailed discussion of the formulation, the main characteristics of the proposed law are illustrated with a number of academic examples for different combinations of mechanical loading and chemical degradation sequences. The model is finally validated against experimental results from the literature consisting of three-point bending tests performed on mortar samples previously exposed to an aggressive solution for different time periods.

1. Introduction

In the numerical analysis of mechanical problems using the Finite Element Method (FEM), it is often convenient to use zero-thickness interface elements to adequately represent cracking. These elements are introduced in between and connected with conventional continuum elements, in order to represent the displacement jumps occurring in a fracture, by using constitutive laws formulated in terms of the normal and tangential components of the stress and the relative displacements between the two faces of the interface element.

Zero-thickness interface elements were originally introduced in the late 1960s and early 1970s, motivated by the need to model discontinuities in rock masses. Based on the proposal by Goodman et al. (1968) and the subsequent improvements in later works (e.g. Ghaboussi et al., 1973; Desai et al., 1984; Gens et al., 1988), the formulation of interface elements has been widely implemented in Finite Element codes and has been applied to many practical problems. For instance, this modelling approach has been used for modelling delamination in composite materials (Chen et al., 1999; Alfano and Crisfield, 2001; Parrinello et al., 2016), the behaviour of soil–structure interfaces (D'Aguiar et al., 2011; Cerfontaine et al., 2015), the dessication cracking of soils (Manzoli et al., 2018; Gui et al., 2018; Pouya et al., 2019), the stability of rock masses (Gens et al., 1988), hydraulic fracturing (Carrier and Granet, 2012; Nguyen et al., 2017; Li et al., 2017; Rueda-Cordero et al., 2019), sanding in hydrocarbon production (Garolera et al., 2019), and fracturing processes in masonry (Lotfi and Shing, 1994; Koutromanos and Shing, 2012; Lourenço, 1996) and concrete (Stankowski et al., 1993a,b; López et al., 2008a,b; Etse et al., 2012; Wang et al., 2020), among other engineering problems.

A fundamental aspect of the formulation of interface elements is the constitutive law, since it characterises the opening/sliding criterion and the subsequent evolution of stresses and relative displacements. For the particular case of quasi-brittle geo-materials, many constitutive laws are based on the Fictitious Crack Model (FCM) proposed by Hillerborg et al. (1976), which introduced a non-linear alternative theory to the classic Linear Elastic Fracture Mechanics to model

* Corresponding author.
E-mail addresses: ariadna.martinez.e@upc.edu (A. Martínez), J.Liaudat@tudelft.nl (J. Liaudat), carlos.maria.lopez@upc.edu (C.M. López), ignacio.carol@upc.edu (I. Carol).

https://doi.org/10.1016/j.ijsolstr.2021.111379
Received 15 June 2021; Received in revised form 25 October 2021; Accepted 23 November 2021
Available online 18 December 2021

the initiation and propagation of cracks. Based on contributions from previous works (Dugdale, 1960; Barenblatt, 1962), the FCM assumes that the physical processes that develop in the fracture process zone, which range from microcracking to the complete formation of the crack, are concentrated along a fictitious line with zero thickness. This approach, initially limited to fractures in Mode I (pure tensile fractures), has later been extended to account for coupled effects of normal/shear loading. Those conceptual models have led to constitutive laws developed within the theoretical framework of damage (Camacho and Ortiz, 1996; Willam et al., 2004), plasticity (Stankowski et al., 1993a; Lotfi and Shing, 1994; Carol et al., 1997; Oliveira and Lourenço, 2004; Puntel et al., 2006; Jacobsen et al., 2013) or a combination of damage and plasticity/friction (Jefferson, 2002; Spada et al., 2009; Alfano et al., 2006). This varied set of laws have made it possible to represent different aspects of the mechanical constitutive behaviour of the interfaces and fractures in quasi-brittle materials.

In particular, the elasto-plastic constitutive law proposed by Carol et al. (1997, 2001) has been successfully used by the group of Material Mechanics (MECMAT) of the Technical University of Catalonia (UPC) for modelling fracturing processes in concrete at the meso-scale under different 2D/3D mechanical loading conditions (López et al., 2008a,b; Caballero et al., 2006). In this meso-mechanical model, the coarser aggregate fraction is explicitly represented as embedded in a mortar matrix. The interface elements are introduced *a priori* along all the contact surfaces between mortar and aggregate continuum elements, and in between some selected mortar–mortar contacts in order to provide sufficient potential cracking paths. This model was later extended to a coupled formulation to consider cracking processes in concrete driven by diffusion processes (Idiart et al., 2011b; Pérez et al., 2013). In Idiart et al. (2011b) the meso-mechanical model was coupled with a moisture diffusion model to simulate cracking due to drying shrinkage of the mortar matrix. The effect of cracking on the diffusion process was explicitly considered by modelling the localised flux along fractures represented by open interface elements using the formulation proposed in Segura and Carol (2004). The differential volume changes that lead to cracking result from imposing volumetric shrinkage to the continuum mortar elements as a function of the relative humidity level. A similar implementation was used in Pérez et al. (2013) to model concrete spalling due to exposure to high temperature, where the diffusion of heat and the differential thermal expansion of the continuum elements representing the mortar matrix and the aggregates are responsible for concrete cracking. In Idiart et al. (2011a), the diffusion model was further developed to simulate the diffusion of aqueous sulfate species from an external source into a concrete specimen and their reaction with the cement paste to form ettringite. The formation of secondary ettringite leads to the expansion of the continuum elements representing the mortar matrix and the consequent cracking of the interface elements. In turn, open cracks constitute preferential paths for the ingress of sulfate species accelerating the degradation process. In this model, chemical reactions were only allowed in the continuum elements representing mortar, i.e. the formation of ettringite inside open cracks was not allowed. This restriction was recently overcome in the diffusion–reaction formulation for interface elements proposed in Liaudat et al. (2020) for simulating concrete cracking due to the Alkali-Silica Reaction (ASR). In this model, the expansive ASR products are formed within the interface elements representing mortar-aggregate contacts and pre-existing fractures in the aggregates. To reproduce the resulting chemo-mechanical coupling, the original constitutive law (Carol et al., 1997, 2001) had to be modified to account for the interplay between the increasing amount of compressible ASR products and the mechanics of fracture formation.

Current efforts in the development of the meso-scale concrete degradation model are focused on diffusion–reaction processes that lead to loss of material strength rather than to differential or localised expansions within the material. This kind of degradation processes may result from the hydrolysis of the cement paste components by soft water or from cation-exchange reactions between aggressive fluids and the cement paste. In particular, a model is being extended to simulate the degradation of oil well cements exposed to carbonated brine in the context of CO_2 capture and storage projects in depleted hydrocarbon reservoirs (IPCC, 2005; Gasda et al., 2004). As a first step, a simple diffusion–reaction model has been proposed by the authors which is able to reproduce the decalcification of the well cement as the carbonic acid diffuses into the material from the surrounding carbonated brine (Liaudat et al., 2018). The decalcification of the cement paste is associated to an increase of porosity and consequent loss of mechanical strength (Kutchko et al., 2007, 2008; Rimmelé et al., 2008; Carey et al., 2007; Duguid and Scherer, 2010). In a second step, the diffusion–reaction formulation will be coupled with the meso-mechanical model. For this purpose, in this paper, a new constitutive law for interface elements is proposed that incorporates the effect of the degradation of the strength parameters of the material due to chemical processes.

The new constitutive law is based on the original formulation by Carol et al. (1997, 2001), but incorporating the softening of the material strength parameters due to chemical degradation via an external history variable updated by the diffusion–reaction model. To the best of the authors' knowledge, no other constitutive law for interface elements in the literature is capable of reproducing the effect of chemical degradation on the fracture mechanics of cement-based materials. The only related antecedents that can be mentioned is the constitutive model proposed by Caggiano and Etse (2015), which includes the effect of exposure to high temperatures on the material softening rules, and the model by Idiart et al. (2011b), which includes material hardening as a function of time.

The paper is structured as follows. After this introduction, in Section 2, the new constitutive law is described in detail. In Section 3, the main characteristics of the law are illustrated with a number of verification examples at the constitutive level for shear–compression and pure tensile loading, combined with different sequences of chemical degradation. Next, in Section 4, the constitutive law is used in two application examples. The first example considers the propagation of a small, initially stable, bending crack in a beam due to the chemical degradation at the tip of the crack. In the second example, three-point bending tests carried out by Le Bellégo et al. (2000) on mortar beams that have been previously exposed during different periods of time, to an aggressive solution. The paper finishes in Section 5 with some concluding remarks.

2. The constitutive model

The constitutive law for interface elements proposed in this paper is an extension of the formulation originally proposed by Carol et al. (1997), and subsequently improved by Carol et al. (2001), López et al. (2008a) and Caballero et al. (2008). This new version of the law introduces the effect of chemical degradation on the mechanical behaviour of interfaces. The model is formulated in the framework of elasto-plasticity and incorporates concepts and material parameters of non-linear fracture mechanics.

2.1. Basic variables

The constitutive behaviour is formulated in terms of one normal and two tangential stress components on the interface mid-plane, $\boldsymbol{\sigma} = \left[\sigma_N \quad \sigma_{L1} \quad \sigma_{L2}\right]^{\mathrm{T}}$, and their conjugate relative separation displacements, $\mathbf{r} = \left[r_N \quad r_{L1} \quad r_{L2}\right]^{\mathrm{T}}$ (T: transpose) (Fig. 1).

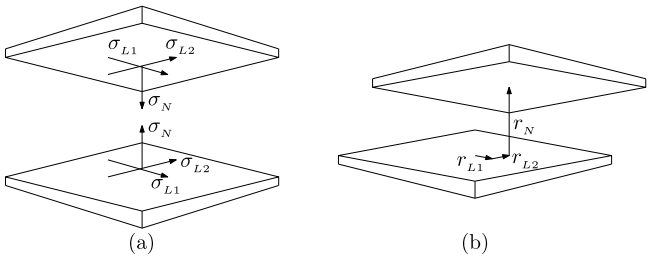

Fig. 1. Definition of (a) stress variables and (b) conjugate relative displacements at a point of the interface mid-plane.

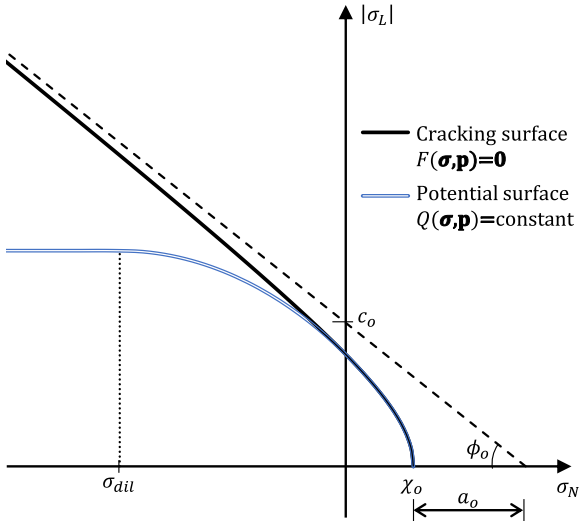

Fig. 2. Cracking surface $F = 0$ and plastic potential Q = constant for non-degraded conditions ($\omega = 0$, $\eta = 0$). The dashed line represents the asymptote to the hyperbola.

2.2. Cracking surface

Cracking begins when the stress on the interface plane reaches the condition $F(\boldsymbol{\sigma}, \mathbf{p}) = 0$, where F is the adopted cracking surface defined in the space of normal and shear stresses, and vector $\mathbf{p}$ collects the current values of the cracking surface parameters. The cracking surface adopted in this paper (Fig. 2) is the same three-parameter hyperbolic surface proposed by Caballero et al. (2008), namely:

$$F(\boldsymbol{\sigma}, \mathbf{p}) = -\left(c - \sigma_N \tan\phi\right) + \sqrt{\sigma_L^2 + (c - \chi \tan\phi)^2} \tag{1}$$

where σ_L is the shear stress intensity ($\sigma_L = \sqrt{\sigma_{L1}^2 + \sigma_{L2}^2}$), χ is the abscissa of the hyperbola representing the tensile strength, c is the apparent cohesion, and $\tan\phi$ is the coefficient of internal friction. The last two parameters define the asymptote to the hyperbola, as shown in Fig. 2.

This hyperbola provides a smooth transition between two limit states (Fig. 3): (i) Mode I cracking, corresponding to cracking under pure tension without shear stresses, when the surface is reached along the horizontal axis; and (ii) asymptotic Mode II cracking (or Mode IIa cracking), corresponding to cracking under shear and very high compression, when the hyperbola tends to a Coulomb criterion.

The parameters of the hyperbola must hold the following relation:

$$c \geq \chi \left(\frac{1}{2\tan\phi} + \tan\phi\right) \tag{2}$$

This condition not only assures a correct definition of the hyperbola but also guarantees that under pure tensile loading the crack is produced in Mode I (in a direction perpendicular to the load) (López, 1999).

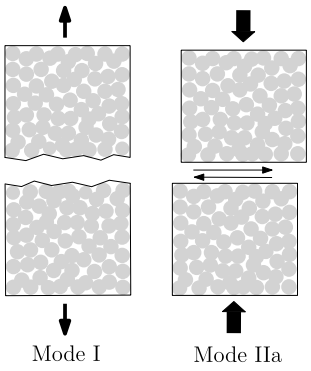

Fig. 3. Fundamental modes of fracture.

In the general loading case, the cracking surface does not remain static but may shrink representing a softening behaviour, as it is discussed in the following Section 2.4. In the original version of the law, the cracking surface was only considered to shrink due to the mechanical degradation associated to the fracture process. In the present paper, in addition to the mechanical degradation, the possibility of softening due to chemical degradation processes is incorporated.

2.3. History variables

The parameters of the hyperbola evolve as functions of two history variables, one internal reflecting the degradation due to the fracture process (ω) which was already in previous versions of the model, and a new one external (η) reflecting the degradation due to chemical processes.

The new external history variable is assumed to result from the simulation of the chemo-transport processes leading to the degradation of the material, and, therefore, for the mechanical constitutive law proposed in this paper, it is considered as a given value. Moreover, η is assumed to be a dimensionless variable, ranging between $\eta = 0$, for a non-degraded material, and $\eta = 1$, for a completely degraded material. Moreover, it is assumed that the degradation process is irreversible ($d\eta \geq 0$), and, therefore, possible healing processes are not considered. Depending on the problem at hand, the variable η may be defined as a function of different history variables of the chemo-transport simulation, such as the concentration of solid phases or the material porosity.

The internal history variable (ω), in contrast, is obtained as a function of the work spent on fracture processes (W^{cr}) in the following incremental form:

$$d\omega = \frac{dW^{cr}}{G_F^I} \tag{3}$$

where G_F^I is the specific fracture energy of the material in Mode I (Fig. 3), which is defined as the amount of energy necessary to create one unit area of a crack under pure tension. This parameter, which in the original law was assumed constant, is now expected to decrease for increasing chemical degradation, at is discussed below (Section 2.4). The increment of work spent in fracture processes is defined as in the original version of the law (Carol et al., 1997), i.e.

$$dW^{cr} = \begin{cases} \boldsymbol{\sigma} \cdot d\mathbf{r}^{cr} & \text{if } \sigma_N \geq 0 \\ \left(\sigma_L - \left|\sigma_N\right| \tan\phi\right) dr_L^{cr} & \text{if } \sigma_N < 0 \end{cases} \tag{4}$$

where $\mathbf{r}^{cr}$ is the vector of crack relative displacements and dr_L^{cr} represents the increment of tangential relative (sliding) displacements ($r_L = \sqrt{r_{L1}^2 + r_{L2}^2}$).

These expressions imply that when the interface element is in tension all the dissipated plastic work goes into the fracture process. In

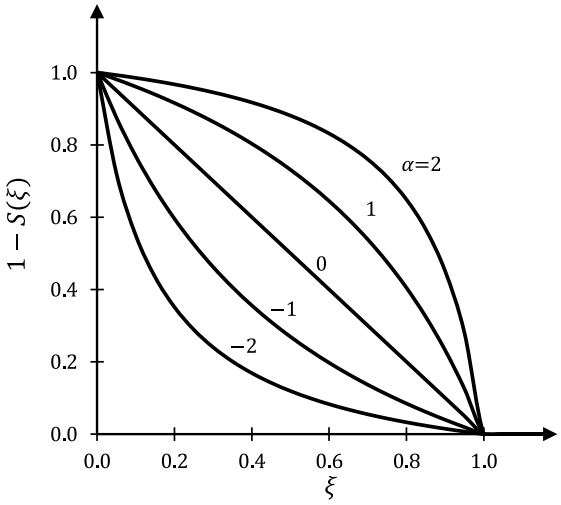

Fig. 4. Scaling function S.

contrast, in compression, the work dissipated also includes a significant component of friction producing heat, which does not contribute to the crack formation and, therefore, it is not accounted in W^{cr} (Willam and Bićanić, 1984).

2.4. Evolution laws

The evolution of the cracking surface $F = 0$ is controlled by the evolution of the surface parameters χ, c and $\tan\phi$ as functions of the history variables ω and η. For the sake of generality, the evolution laws of these parameters are defined using the scaling function $S(\xi)$ (Fig. 4), defined as follows:

$$S(\xi,\alpha) = \begin{cases} \dfrac{\xi e^{-\alpha}}{1+\xi(e^{-\alpha}-1)} & \text{if } \xi < 1 \\ 1 & \text{if } \xi \geq 1 \end{cases} \tag{5}$$

where ξ is an intermediate function of ω or η, to be defined below for each material parameter, and α is a shape coefficients that may be different for each definition of ξ. As a first approach or in the absence of sufficient information, the shape coefficients can be taken to be equal to 0 to obtain linear softening laws, i.e. $S(\xi) = \xi$.

2.4.1. Evolution of tensile strength (χ)

The tensile strength parameter χ is reduced from its initial (non-degraded) value χ_o by means of the following softening law:

$$\chi = \chi_o \left[1 - S(\xi_\chi^\omega, \alpha_\chi^\omega)\right]\left[1 - S(\xi_\chi^\eta, \alpha_\chi^\eta)\right] \tag{6}$$

The first factor in square brackets accounts for the effect of the fracture work, while the second factor accounts for the effect of chemical degradation. Note that the tensile strength will vanish either for $\xi_\chi^\omega = 1$ or for $\xi_\chi^\eta = 1$. The intermediate variable ξ_χ^ω is obtained as the integral of the history variable increments $d\omega$, given by Eq. (3), over the loading process, i.e.:

$$\xi_\chi^\omega = \int d\omega = \int \frac{dW^{cr}}{G_F^I} \tag{7}$$

As mentioned above, it may be expected that the chemical degradation will reduce the specific fracture energy of the material. In order to introduce this effect, it is assumed that G_F^I varies as a function of the chemical degradation according to the following expression:

$$G_F^I = \left[1 - S(\xi_G^\eta, \alpha_G^\eta)\right] G_{Fo}^I + S(\xi_G^\eta, \alpha_G^\eta) G_{Fr}^I \tag{8}$$

where G_{Fo}^I and G_{Fr}^I are material parameters corresponding to the non-degraded and the completely degraded values of G_F^I, respectively.

In both Eqs. (6) and (8), the intermediate variables representing the chemical degradation are assumed to be equal to the history variable η, i.e.

$$\xi_\chi^\eta = \xi_G^\eta = \eta \tag{9}$$

2.4.2. Evolution of the internal friction coefficient ($\tan\phi$)

The coefficient of internal friction diminishes from the initial value $\tan\phi_o$ to the residual value $\tan\phi_r$, according to:

$$\tan\phi = \left[1 - S(\xi_\phi^\omega, \alpha_\phi^\omega)\right] \tan\phi_o + S(\xi_\phi^\omega, \alpha_\phi^\omega) \tan\phi_r \tag{10}$$

where ξ_ϕ^ω is an intermediate variable and α_ϕ^ω the corresponding shape coefficient. The intermediate variable is defined as follows:

$$\xi_\phi^\omega = \int \frac{dW^{cr}}{G_F^{IIa}} = \frac{G_{Fo}^I}{G_{Fo}^{IIa}} \int \frac{dW^{cr}}{G_F^I} = \frac{G_{Fo}^I}{G_{Fo}^{IIa}} \int d\omega \tag{11}$$

where G_{Fo}^{IIa} is the initial value of the specific fracture energy in Mode IIa. This expression corresponds to assuming that the chemical degradation of the specific fracture energy in Mode IIa occurs in the same proportion as for G_F^I, in such a way that:

$$\frac{G_F^I}{G_F^{IIa}} = \frac{G_{Fo}^I}{G_{Fo}^{IIa}} \tag{12}$$

for any value of η. From Eqs. (10) and (11), it follows that, in the absence of chemical degradation ($\eta = 0$), friction angle reaches its residual value when the work spent in the fracture process (W^{cr}) is equal to G_{Fo}^{IIa}.

2.4.3. Evolution of the apparent cohesion (c)

In order to avoid inconsistent behaviour in the tension/shear zone, the evolution of the apparent cohesion is linked to the evolution of the tensile strength and of the coefficient of internal friction by means of the following expression (López, 1999):

$$c = (\chi + a)\tan\phi \tag{13}$$

where a is an auxiliary variable representing the horizontal distance between the vertex of the hyperbola and the intersection point of the asymptotes with the horizontal axis (Fig. 2). This auxiliary variable is considered to evolve according to:

$$a = \left(\frac{c_o}{\tan\phi_o} - \chi_o\right)\left[1 - S(\xi_a^\omega, \alpha_a^\omega)\right] \tag{14}$$

where the intermediate variable used in the scaling function S is $\xi_a^\omega = \xi_\phi^\omega$ and α_a^ω is the corresponding shape coefficient. Note that a, as well as $\tan\phi$, only depends on η indirectly through G_F^I (Eqs. (11),(7) and (8)).

2.4.4. Evolution of the cracking surface

The overall evolution of the cracking surface is uniquely defined by the evolution laws presented in previous sections. However, for illustrative purposes, let us consider the evolution of the cracking surface in three particular cases.

In the first case, an increasing normal aperture is imposed to the interface element (Mode I) without any chemical degradation ($\eta = 0$). Under these conditions, the cracking surface is eventually reached at the tip of the hyperbola. At this point, the material starts to crack and, for increasing normal aperture, the history variable ω grows from 0 until reaching a value of 1, when $W^{cr} = G_{Fo}^I$. As a consequence, tensile strength vanishes, while (for typical values of $G_{Fo}^{IIa}/G_{Fo}^I \approx 10$ and shape coefficients $-2 < \alpha < 2$) c and $\tan\phi$ are only slightly reduced. The net result is that the initial surface (black line in Fig. 5) is shifted to the left and slightly shrunken (blue line in Fig. 5). Note that after cracking in tension, any additional prescribed opening displacements would directly become plastic, opening further the interface crack under zero normal stress without generating any changes in the history variable ω.

In the second case, a very high normal compression load is applied, followed by an increasing shear displacement (Mode IIa). Again, no

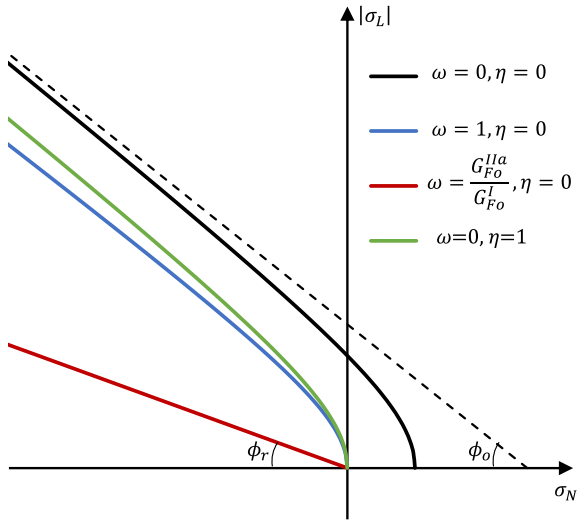

Fig. 5. Evolution of the cracking surface $F = 0$. (For interpretation of the references to colour in this figure legend, the reader is referred to the web version of this article.)

chemical degradation is considered ($\eta = 0$). Under these conditions, the cracking surface is reached at the asymptotic region of the hyperbola, and a shear–compression crack is developed. As work is spent in the fracture process, the cracking surface evolves in two different stages. In the first stage, the surface shrinks and shifts to the left as in the previous pure tension case, until reaching the configuration indicated with a blue line in Fig. 5, when $\omega = 1$. In the second stage, the surface only shrinks, degenerating into a pair of straight lines (red line in Fig. 5), representing the residual friction capacity of the fully opened and shear smoothed interface, when $\omega = G_{Fo}^{IIa}/G_{Fo}^{I}$.

In the last case, the interface is exposed to chemical degradation ($\eta > 0$) without any simultaneous mechanical loading. Under this condition, there is no work spent in fracture processes ($\omega = 0$), and, therefore, the only parameter of the hyperbola that is reduced is the tensile strength, which vanishes for $\eta = 1$. As a consequence, the initial cracking surface (black line in Fig. 5) only shifts to the left, reaching the position indicated with the green line in Fig. 5.

2.5. Flow rule

In the framework of elasto-plasticity, the direction of inelastic deformations of the crack (i.e., the proportion between normal opening and shear slip of the crack) at any time of the loading history is assumed to be perpendicular to a 'potential surface' $Q = constant$, which is defined in the same space as the cracking surface $F = 0$. If, at a given point, the direction of the gradient of $Q = constant$ coincides with direction of the gradient of $F = 0$, the flow rule is associated; otherwise, it is non-associated.

For the present model, the normal direction of the fracture potential surface ($\mathbf{m}$) is defined as follows:

$$\mathbf{m} = \frac{\partial Q}{\partial \boldsymbol{\sigma}} = \mathbf{A}\mathbf{n} \tag{15}$$

where $\mathbf{n}$ is the gradient of F, i.e.,

$$\mathbf{n} = \frac{\partial F}{\partial \boldsymbol{\sigma}} = \begin{bmatrix} \frac{\partial F}{\partial \sigma_N} \\ \frac{\partial F}{\partial \sigma_{L1}} \\ \frac{\partial F}{\partial \sigma_{L2}} \end{bmatrix} = \begin{bmatrix} \tan\phi \\ \frac{\sigma_{L1}}{\sqrt{\sigma_L^2 + (c - \chi\tan\phi)^2}} \\ \frac{\sigma_{L2}}{\sqrt{\sigma_L^2 + (c - \chi\tan\phi)^2}} \end{bmatrix} \tag{16}$$

and $\mathbf{A}$ is a transformation matrix. If $\mathbf{A}$ is equal to the identity tensor ($\mathbf{A} = \mathbf{I}$), the potential surface coincides with the cracking surface and the flow is associated; otherwise ($\mathbf{A} \neq \mathbf{I}$), it is non-associated.

In the context of frictional materials, the angle of vector $\mathbf{m}$ with the vertical (shear) axis can be interpreted as the current dilatancy angle exhibited by the model. Therefore, a direction parallel to the vertical axis indicates no dilatancy at all, while a direction parallel to the horizontal axis indicates normal opening of the crack with no shear slip, as it is obtained under pure tension.

In heterogeneous materials such as concrete or rock, dilatancy represents the well-known tendency of the two faces of the crack under zero or low normal compression, to dilate when sliding takes place, because of the well-known 'saw tooth effect'. However, dilatancy diminishes with the level of compression, and finally disappears at very high levels of compression (Atkinson et al., 1989). In addition, dilatancy decreases as sliding progresses (Pande et al., 1990) and the crack surface is degraded by the fracture process.

In order to introduce these effects, the transformation matrix $\mathbf{A}$ is defined as follows:

$$\mathbf{A} = \begin{bmatrix} f_{dil}^{\sigma} f_{dil}^{\omega} & 0 & 0 \\ 0 & 1 & 0 \\ 0 & 0 & 1 \end{bmatrix} \tag{17}$$

where f_{dil}^{σ} and f_{dil}^{ω} are dimensionless factors varying between 1 and 0, which account for the reduction of dilatancy due to the applied compressive stress and the mechanical degradation of the interface, respectively. These factors are given by the following expressions:

$$f_{dil}^{\sigma} = 1 - S\left(\xi_{dil}^{\sigma}, \alpha_{dil}^{\sigma}\right) \tag{18}$$

$$f_{dil}^{\omega} = 1 - S\left(\xi_{dil}^{\omega}, \alpha_{dil}^{\omega}\right) \tag{19}$$

where the intermediate variable ξ_{dil}^{σ} is given by:

$$\xi_{dil}^{\sigma} = \begin{cases} 0 & \text{if } \sigma_N \geq 0 \\ \dfrac{|\sigma_N|}{\sigma_{dil}} & \text{if } \sigma_N < 0 \end{cases} \tag{20}$$

and the intermediate variable ξ_{dil}^{ω} is given by Eq. (11) (i.e. $\xi_{dil}^{\omega} = \xi_{\phi}^{\omega}$). α_{dil}^{σ} and α_{dil}^{ω} are the corresponding shape coefficients for the scaling function S. In Eq. (20), σ_{dil} is a pre-established material parameter corresponding to the compression stress value beyond which the dilatancy is completely suppressed. Note that by reducing G_F^{IIa}, the chemical degradation will indirectly reduce the dilatancy (Eqs. (11), (7) and (8)).

In Fig. 2, the potential surface corresponding to the initial state ($\omega = 0$, $\eta = 0$) is depicted. Note that in this state, the flow rule is associated for $\sigma_N \geq 0$ and non-associated for $\sigma_N < 0$.

2.6. Constitutive rate equation

The relative displacement vector ($\mathbf{r}$) may be expressed as the sum of a recoverable (elastic) component ($\mathbf{r^{el}}$), and a non-recoverable (plastic) component ($\mathbf{r^{cr}}$):

$$r_i = r_i^{el} + r_i^{cr} \tag{21}$$

The constitutive relationship of the interface is given by:

$$\sigma_i = K_{ij}^{o} r_j^{el} = K_{ij}^{o}(r_j - r_j^{cr}) \tag{22}$$

where $\mathbf{K}^o$ is assumed to be a diagonal matrix with constant coefficients K_N^o and K_L^o for the normal and shear degrees of freedom, respectively. These coefficients should simply be interpreted as penalty coefficients that must be set to values as high as possible without causing numerical difficulties. Therefore, K_N^o and K_L^o are constant parameters that are not affected by the chemical degradation. The non-recoverable component of the relative displacement increment vector may be written as follows:

$$dr_j^{cr} = m_j d\lambda \tag{23}$$

where λ is the plastic multiplier and m_j is the gradient of the potential surface Q, as defined in Eq. (15). The increment of the plastic multiplier $d\lambda$ can be either positive in combination with $F = 0$ ('consistency

condition' for plastic loading) or zero in combination with $F < 0$ (elastic unloading). That means that the three following (Kuhn–Tucker) conditions must be met simultaneously:

$$d\lambda \geq 0; \quad dF \leq 0; \quad dF d\lambda = 0 \tag{24}$$

In the case of a plastic loading increment ($d\lambda > 0$), the so-called consistency condition applies:

$$dF = \frac{\partial F}{\partial \sigma_i} d\sigma_i - H d\lambda + \frac{\partial F}{\partial \eta} d\eta = 0 \tag{25}$$

with

$$H = -\frac{\partial F}{\partial \lambda} = -\frac{\partial F}{\partial p_i}\frac{\partial p_i}{\partial \omega}\frac{\partial \omega}{\partial r_j^{cr}} m_j \tag{26}$$

and

$$\frac{\partial F}{\partial \eta} = \frac{\partial F}{\partial p_i}\frac{\partial p_i}{\partial \eta} \tag{27}$$

H is the hardening/softening parameter, which reflects the variation of shape and position of the cracking surface due to the work spent in fracture processes. Note in Eq. (26) that $\partial F/\partial\lambda$ is always a negative value which leads to a contraction (softening) of the cracking surface driven by the evolution of the parameters (p_i) as functions of the history variable ω. In turn, the term $\partial F/\partial\eta$ introduces an additional softening of the cracking surface as a consequence of the chemical degradation of the parameters of the hyperbola.

Combining Eqs. (21), (23), (25) and (27), the increment of the plastic multiplier may be expressed as:

$$d\lambda = \frac{n_k K^o_{kj} dr_j + \dfrac{\partial F}{\partial p_i}\dfrac{\partial p_i}{\partial \eta} d\eta}{H + n_p K^o_{pq} m_q} \tag{28}$$

where n_i is the normal to the cracking surface already defined in Eq. (16). Finally, the incremental constitutive equation which establishes the relationship between stress and relative displacements of the interface is given as follows:

$$d\sigma_i = \left[K^o_{ij} - \frac{K^o_{ik} m_k n_l K^o_{lj}}{H + n_p K^o_{pq} m_q}\right] dr_j - \frac{K^o_{ij} m_j \dfrac{\partial F}{\partial p_r}\dfrac{\partial p_r}{\partial \eta}}{H + n_p K^o_{pq} m_q} d\eta \tag{29}$$

2.7. Constitutive integration

The above-described differential equations are numerically integrated using the backward Euler discretisation rule. The resulting system of non-linear equations is solved with the Newton–Raphson iterative method. The procedure is similar to that used for the original constitutive law (Carol et al., 1997), which is extensively discussed by Caballero (2005) and Caballero et al. (2008). In addition, in order to reduce the integration errors and allow bigger global loading steps, an automatic substepping scheme is adopted for the most restrictive Gauss points. Inspired by the proposal of Marques (1984), the size of each sub-step is determined with a double control procedure, using a radial criterion that limits the distance of the elastic predictor from the fracture surface, and a tangential criterion that controls the change of direction of the flow rule. Further details of the sub-stepping procedure can be found in Carol et al. (2001).

A negative side effect of the substepping technique is that, in principle, the tangent operator $d\boldsymbol{\sigma}/d\boldsymbol{\Delta}\mathbf{r}$ evaluated at the end of the loading step is not consistent with the adoption of an implicit (backward Euler or mid-point) rule for the solution of the elastoplastic boundary value problem. As a result, the quadratic convergence of a full Newton–Raphson linearisation may be lost. This shortcoming is overcome by applying the recursive procedure developed by Caballero et al. (2008), based on a previous work by Pérez-Foguet et al. (2001), to obtain a consistent tangent operator in interface elastoplastic constitutive laws with substepping schemes. For the sake of completeness, in the following paragraphs, the overall procedure for the integration of the elastoplastic constitutive relations is briefly summarised.

The total increments of relative displacement, $\boldsymbol{\Delta}\mathbf{r}$, and chemical degradation, $\Delta\eta$, to be applied in the considered step, are subdivided in N (not necessarily equal) subincrements $\boldsymbol{\Delta}\mathbf{r}_k$ and $\Delta\eta_k$ such that:

$$\boldsymbol{\Delta}\mathbf{r}_k = \mathbf{r}_k - \mathbf{r}_{k-1} = \alpha_k \boldsymbol{\Delta}\mathbf{r} \tag{30}$$

$$\Delta\eta_k = \eta_k - \eta_{k-1} = \alpha_k \Delta\eta \tag{31}$$

with

$$\sum_{k=1}^{N} \alpha_k = 1 \text{ and } 0 < \alpha_k < 1 \tag{32}$$

For each substep, the corresponding increment of stress, $\boldsymbol{\Delta\sigma}_k = \boldsymbol{\sigma}_k - \boldsymbol{\sigma}_{k-1}$, is obtained by solving the following system of non-linear equations:

$$\mathbf{f}(\mathbf{x}_k) = \begin{bmatrix} \boldsymbol{\Delta\sigma}_k + \Delta\lambda_k \mathbf{K}^o \mathbf{m}_k - \mathbf{K}^o \boldsymbol{\Delta}\mathbf{r}_k \\ \Delta\omega_k - \dfrac{\Delta\lambda_k h_k}{G^I_{F_k}} \\ F\left(\boldsymbol{\sigma}_k, \mathbf{p}(\omega_k, \eta_k)\right) \end{bmatrix} = \mathbf{0} \tag{33}$$

where $\Delta\omega_k = \omega_k - \omega_{k-1}$, $\Delta\lambda_k = \lambda_k - \lambda_{k-1}$, and $h = \partial W^{cr}/\partial\lambda$ is the plastic modulus. This system of equations is solved *via* the Newton–Raphson method, adopting $\boldsymbol{\sigma}_k$, λ_k, and ω_k as the independent variables, i.e. the unknown vector is $\mathbf{x}_k = \begin{bmatrix}\boldsymbol{\sigma}_k & \omega_k & \lambda_k\end{bmatrix}^{\mathsf{T}}$. According to the Newton–Raphson method, an approximate solution vector ${}^i\mathbf{x}_k$, obtained at iteration i, is improved during iteration $i+1$ by means of a correction ${}^{i+1}\delta\mathbf{x}$, such that ${}^{i+1}\mathbf{x}_k = {}^i\mathbf{x}_k + {}^{i+1}\delta\mathbf{x}$. The corrective vector is obtained by solving the following system of linear equations:

$${}^{i+1}\delta\mathbf{x} = -\left(\frac{\partial \mathbf{f}({}^i\mathbf{x}_k)}{\partial \mathbf{x}}\right)^{-1} \mathbf{f}({}^i\mathbf{x}_k) \tag{34}$$

where $\mathbf{f}({}^i\mathbf{x}_k)$ is the residual vector after iteration i, and the gradient of the residual vector corresponds to the Jacobian matrix:

$${}^i\mathbf{J}_k = \begin{bmatrix} \mathbf{I}_3 + \Delta\lambda \mathbf{K}^o \dfrac{\partial \mathbf{m}}{\partial \boldsymbol{\sigma}} & \Delta\lambda \mathbf{K}^o \dfrac{\partial \mathbf{m}}{\partial \omega} & \mathbf{K}^o \mathbf{m} \\ -\dfrac{\Delta\lambda}{G^I_F}\dfrac{\partial h}{\partial \boldsymbol{\sigma}} & 1 - \dfrac{\Delta\lambda}{G^I_F}\dfrac{\partial h}{\partial \omega} & -\dfrac{h}{G^I_F} \\ \dfrac{\partial F}{\partial \boldsymbol{\sigma}} & \dfrac{\partial F}{\partial \omega} & 0 \end{bmatrix}_{\mathbf{x}={}^i\mathbf{x}_k} \tag{35}$$

The consistent tangent operator $d\boldsymbol{\sigma}/d\boldsymbol{\Delta}\mathbf{r}$, evaluated at the end of the loading step is obtained by applying the following expression (Caballero et al., 2008; Pérez-Foguet et al., 2001):

$$\frac{d\boldsymbol{\sigma}}{d\boldsymbol{\Delta}\mathbf{r}} = \mathbf{P}^{\mathsf{T}} \left[\sum_{k=1}^{N} \left(\alpha_k \prod_{j=N}^{k} \mathbf{R}_j\right)\right] \mathbf{P}\mathbf{K}^o \tag{36}$$

with

$$\mathbf{R}_k = \left(\mathbf{J}_k\right)^{-1} \begin{bmatrix} \mathbf{I}_4 & \mathbf{0}_{4\times1} \\ \mathbf{0}_{1\times4} & 0 \end{bmatrix} \tag{37}$$

$$\mathbf{P}^{\mathsf{T}} = \begin{bmatrix} \mathbf{I}_3 & \mathbf{0}_{3\times2} \end{bmatrix} \tag{38}$$

where $\mathbf{J}_k$ is the Jacobian matrix at the end to the kth subincrement (Eq. (35)), evaluated using the converged solution vector $\mathbf{x}_k$. $\mathbf{I}_a$ is the $a \times a$ identity matrix and $\mathbf{0}_{a\times b}$ is a null rectangular matrix with a rows and b columns.

2.8. Summary of model parameters

In the most general case, the proposed constitutive model requires 17 parameters:

- Normal and tangential elastic stiffness (penalty coefficients): K^o_N, K^o_L
- Initial (non-degraded) material parameters χ_o, c_o, $\tan\phi_o$, G^I_{Fo}, G^{IIa}_{Fo}, σ_{dil}
- Degraded material parameters: $\tan\phi_r$, G^I_{Fr}

- Shape parameters of the evolution laws: α_{χ}^{ω}, α_{a}^{ω}, α_{ϕ}^{ω}, α_{χ}^{η}, α_{G}^{η}, α_{dil}^{σ}, α_{dil}^{ω}

The parameters of the original model, i.e. those corresponding to the non-degraded state ($\eta = 0$), can be directly determined or back-calculated, for a given cement-based material, from conventional mechanical tests such as uniaxial compression, indirect tensile tests, triaxial tests, Wedge Splitting Tests, etc. See, for instance, López et al. (2008a,b), López (1999) and Caballero et al. (2007).

The proposed model only adds to the original law one material parameter (G_{Fr}^{I}) and two shape parameters (α_{χ}^{η}, α_{G}^{η}). These parameters will depend not only on the consider cement-based material, but also on the characteristics of the chemical degradation process. For instance, if the cement-based material is exposed to an aggressive fluid, the composition of the fluid will determine which solid phases may be affected and which may not. In turn, the amount and arrangement of these solid phases in the microstructure of the cement-base material will determine how the chemical degradation will affect the macroscopic mechanical response of the material. Therefore, parameters G_{Fr}^{I}, α_{χ}^{η}, and α_{G}^{η} would strictly require to be calibrated against mechanical tests performed on specimens of the same cement-based material which have been degraded under the same exposure conditions which are going to be analysed with the model.

3. Constitutive verification

In order to illustrate the main characteristics of the constitutive model, various numerical examples at the constitutive level are reported in this section. To this end, the constitutive model is used in the case of a zero-thickness interface element which connects the six vertex nodes of two triangular faces in 3D. For the finite element formulation of zero-thickness interface elements, the reader is referred to earlier works (Goodman et al., 1968; Rots, 1988; Gens et al., 1988; Plesha, 1987; Gens et al., 1995). The verification examples below include interface material tests in pure tension and shear under compression, combined with different sequences of chemical degradation. The model parameters used are the following: $K_{N}^{o} = K_{L}^{o} = 1 \times 10^{8}$ MPa/m, $\chi_{o} = 3$ MPa, $c_{o} = 7$ MPa, $\tan\phi_{o} = 0.8785$, $G_{Fo}^{I} = 3 \times 10^{-5}$ MN/m, $G_{Fo}^{IIa} = 10 \times G_{Fo}^{I}$, $\sigma_{dil} = 1$ MPa, $\tan\phi_{r} = 0.4$, $G_{Fr}^{I} = 0.1 \times G_{Fo}^{I}$, $\alpha_{\chi}^{\omega} = \alpha_{a}^{\omega} = \alpha_{\phi}^{\omega} = \alpha_{\chi}^{\eta} = \alpha_{G}^{\eta} = \alpha_{dil}^{\sigma} = \alpha_{dil}^{\omega} = 0$.

3.1. Pure tension

Five different cases of pure tensile loading combined with chemical degradation are tested. For comparison purposes, the constitutive response of a purely mechanical Reference Test, without any chemical degradation, is also provided. The time sequence of the imposed normal relative displacements (r_{N}) and chemical degradation (η) for each test is indicated on the left-hand side plots of Figs. 6 and 7. The respective constitutive responses in terms of σ_{N}-r_{N} diagrams are given on the right-hand side plots of the same figures. Note that because the adopted chemical degradation rates are arbitrary, time is given as a dimensionless variable.

In Tests 1 and 2 (Fig. 6), a normal relative displacement (r_{N}) is initially imposed (without chemical degradation) until reaching the initial tensile strength value χ_{o} (point 'a' in Fig. 6). From this moment, r_{N} and the chemical degradation history variable (η) are increased at constant rates. The rate of r_{N} is the same in both cases, but the rate of η is higher in Test 2 than in Test 1. By comparing the Reference Test with Tests 1 and 2, it can be seen that the greater the rate of chemical degradation, the greater the softening of the interface with the imposed normal aperture.

In Test 3 (blue line in Fig. 6), an initial normal aperture (without chemical degradation) is also imposed, but in this case it is small enough to not reach the cracking surface, i.e. $\sigma_{N} < \chi_{o}$ (point 'b' in Fig. 6). Then, while maintaining the normal relative displacement initially imposed, a constant chemical degradation rate is imposed until the value of $\eta = 0.6$. As η is increased, the cracking surface shrinks progressively, eventually reaching the constant stress state point on the σ_{N} axis and, consequently, the material starts to crack and the normal stress is reduced to $\sigma_{N} = 0.4\chi_{o}$ (point 'c' in Fig. 6). From this moment, a progressive increase of r_{N} is imposed, without additional chemical degradation, which leads to material softening due only to the work spent in the fracture process (W^{cr}).

In Tests 4 and 5 (Fig. 7), a normal relative displacement is initially imposed until reaching point 'b' of the softening branch. Then, keeping r_{N} constant, a different chemical degradation is applied in each case: $\eta = 0.4$ in Test 4 and $\eta = 0.6$ in Test 5. As a consequence, σ_{N} descends to point 'c' in Test 4 and to point 'd' in Test 5 (Fig. 7). From these points, r_{N} is progressively increased in both cases without additional chemical degradation, leading to further softening of the material only due to the work spent in the fracture process.

3.2. Shear under constant compression

Five different cases of shear–compression loading combined with chemical degradation are tested. For comparison purposes, the constitutive response of a purely mechanical Reference Test, without any chemical degradation, is also provided. In all tests, a compression stress $\sigma_{N} = -2$ MPa is initially imposed before any chemical degradation or tangential relative displacement is applied. Note that no shear dilation is possible since $\sigma_{N} < -\sigma_{dil}$ (Eq. (20). The time sequence of the relative displacements (r_{L}) and the chemical degradation (η) for each test is indicated in the left-hand side plots of Figs. 8 and 9. The respective constitutive responses in terms of σ_{L}-r_{L} diagrams are given in the right-hand side plots of the same figures. In addition, the evolution of the cracking surface $F = 0$ for three of those tests is depicted in Fig. 10.

Let us first consider the Reference Test. In this test, once the normal compression stress has been applied, an increasing tangential relative displacement is imposed, without any chemical degradation. In the elastic part of the constitutive response, the tangential stress rapidly increases until reaching the cracking surface $F = 0$ (point 'a' in Figs. 8 and 9). From this point on, the imposed tangential relative displacement induces the propagation of a Mode II crack with consequent reduction of the tangential stress (softening). Note that there is a discontinuity in the slope of the softening branch corresponding to the exhaustion of the tensile strength of the material ($\chi = 0$) when $\xi_{\chi}^{\omega} = 1$ (or, equivalently in this case, when $W^{cr} = G_{Fo}^{I}$). Additional increase of r_{L} causes an additional reduction of σ_{L}, which eventually would reach the residual, pure frictional, shear strength $\sigma_{L} = \left|\sigma_{N}\right| \tan\phi_{r}$ when $\xi_{\phi}^{\omega} = \xi_{a} i^{\omega} = 1$ (or, equivalently in this case, when $W^{cr} = G_{Fo}^{IIa}$).

In Tests 1 and 2 (Fig. 8), an initial relative shear displacement is imposed, without chemical degradation, until the cracking surface $F = 0$ is reached (point 'a' in Fig. 8). From this moment, the increase of r_{L} is accompanied by the increase of the chemical degradation, until reaching $\eta = 1$. The imposed chemical degradation rate in Test 2 is higher than in Test 1, which explains the more pronounced softening behaviour.

In Test 3 (Fig. 8), an initial relative displacement is also imposed but in this case without reaching the cracking surface (point 'b' in Fig. 8). Then, keeping r_{L} constant, the chemical degradation is progressively increased. As a consequence, the cracking surface shifts and shrinks, eventually 'touching' the stress state point (point 'b', Fig. 10, left). A Mode II crack starts to propagate and, as η continues growing, the tangential stress is reduced and part of the imposed tangential relative displacement becomes inelastic. For $\eta = 1$, the tensile strength is exhausted ($\chi = 0$) and the stress point 'c' in Figs. 8 and 10, left, is reached. From this moment, the imposed increase of r_{L} causes a further reduction of the tangential stress until practically reaching the residual shear stress ($\sigma_{L} = \left|\sigma_{N}\right| \tan\phi_{r}$) for $r_{L} = 0.09$ (point 'd' in Figs. 8 and 10, left)

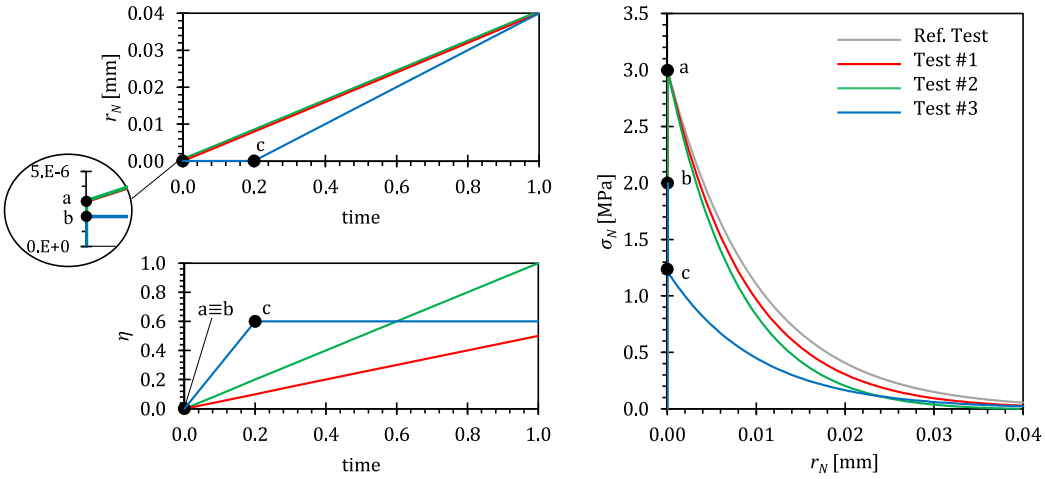

Fig. 6. Pure tension tests combined with chemical degradation (Tests 1–3). For comparison, a Reference Test without chemical degradation is plotted in grey. Upper-left and bottom-left plots depict the time evolution of the imposed normal relative displacement and chemical degradation, respectively. The right plot depicts the normal stress versus the relative normal (opening) displacement. (For interpretation of the references to colour in this figure legend, the reader is referred to the web version of this article.)

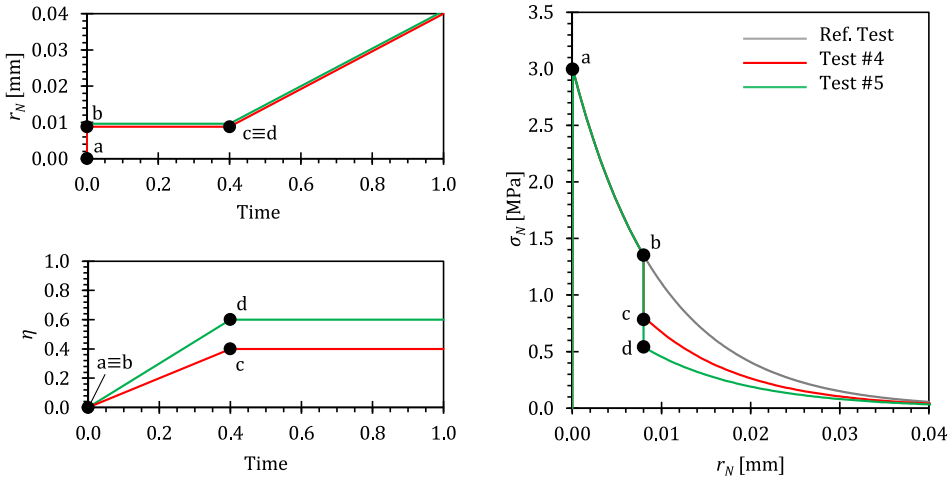

Fig. 7. Pure tension tests combined with chemical degradation (Tests 4 and 5). For comparison, a Reference Test without chemical degradation is plotted in grey. Upper-left and bottom-left plots depict the time evolution of the imposed normal relative displacement and chemical degradation, respectively. The right plot depicts the normal stress versus the relative normal displacement. (For interpretation of the references to colour in this figure legend, the reader is referred to the web version of this article.)

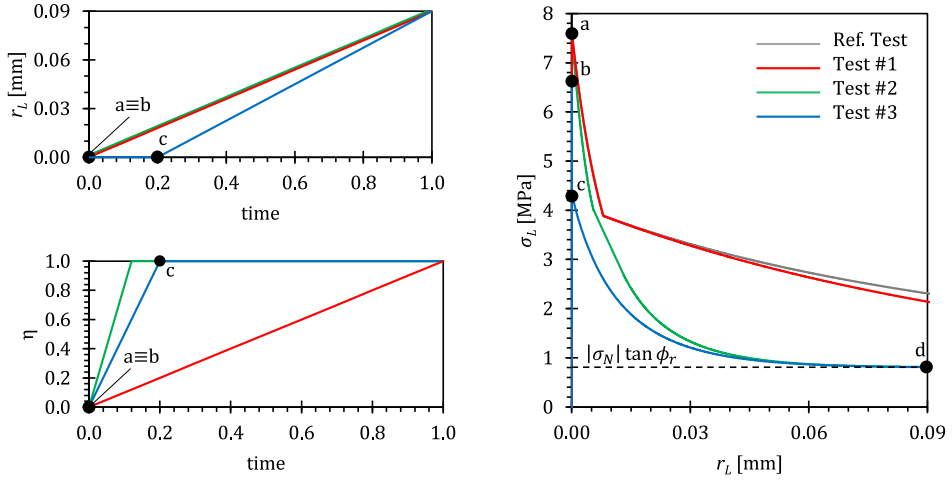

Fig. 8. Shear under compression tests combined with chemical degradation (Tests 1–3). For comparison, a Reference Test without chemical degradation is plotted in grey. The imposed compression stress is in all cases $\sigma_N = -2$ MPa. Upper-left and bottom-left plots depict the time evolution of the imposed tangential relative displacement and chemical degradation, respectively. The right plot depicts the tangential stress versus the relative tangential displacement. (For interpretation of the references to colour in this figure legend, the reader is referred to the web version of this article.)

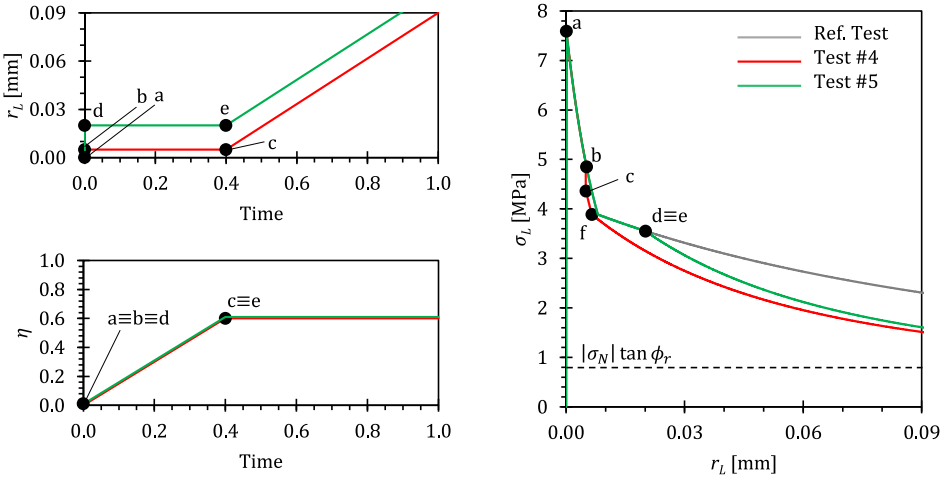

Fig. 9. Shear under compression tests combined with chemical degradation (Tests 4 and 5). For comparison, a Reference Test without chemical degradation is plotted in grey. The imposed compression stress is in all cases $\sigma_N = -2$ MPa. Upper-left and bottom-left plots depict the time evolution of the imposed tangential relative displacement and chemical degradation, respectively. The right plot depicts the tangential stress versus the relative tangential displacement. (For interpretation of the references to colour in this figure legend, the reader is referred to the web version of this article.)

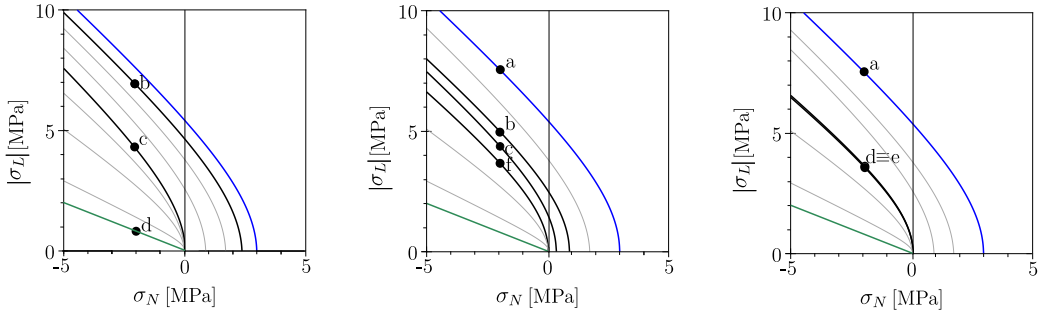

Fig. 10. Evolution of the cracking surface for shear under compression tests combined with chemical degradation. Left, Test 3. Centre, Test 4. Right, Test 5. The blue line corresponds to the initial, non-degraded condition while the green line corresponds to the completely degraded, pure frictional, condition. (For interpretation of the references to colour in this figure legend, the reader is referred to the web version of this article.)

In Tests 4 and 5 (Fig. 9), an initial tangential relative displacement is imposed until a certain point in the softening branch. In Test 4, this point is before the tensile strength is completely exhausted (point 'b' in Figs. 9 and 10, centre), while in Test 5 it is after the tensile strength has been completely exhausted (point 'd' in Figs. 9 and 10, right). Then, in both tests, a chemical degradation of $\eta = 0.6$ is imposed while maintaining r_L constant. In Test 4, the cracking surface shifts to the left because of the increase of η and, consequently, σ_L is reduced (point 'c' in Figs. 9 and 10, centre). In Test 5, in contrast, since the tensile strength is already null and no fracture work is performed, the cracking surface is not altered by the chemical degradation, and the stress state remains the same (point 'e' in Figs. 9 and 10, right). Finally, in both cases, r_L is increased without additional chemical degradation, causing further reduction of the shear stress driven by the work spent in the fracture process. In Test 5, this reduction is only due to the shrinkage of the cracking surface driven by the work spent in the fracture process. In Test 4, in contrast, since there is some remaining tensile strength, the cracking surface first simultaneously shifts and contracts, until the tensile strength vanishes (point 'f' in Figs. 9 and 10, centre), and, thereafter, it only contracts. As in the Reference Test, if the r_L is indefinitely increased in Tests 4 and 5, the shear stress would eventually reach the residual value $\sigma_L = |\sigma_N| \tan \phi_r$.

4. Application examples

In this section, the proposed constitutive law is used for two application examples. The first example is intended to simulate the propagation of an initially stable flexural crack in a beam, due to the chemical degradation of the crack tip. The second example reproduces the experimental bending tests performed by Le Bellégo et al. (2000) on chemically degraded mortar specimens.

4.1. Subcritical cracking due to chemical degradation

Consider an un-reinforced concrete bean subject to bending. Consider also that the most tensioned (bottom) fibre of this structural element is in contact with acidic water (e.g. acidic sewage water) capable of chemically degrading the cement binder by dissolving the calcium bearing solid-phases. In these conditions, the chemical degradation of the bulk concrete will progress as a uniform degradation front from the water–concrete interface towards the interior of the element, typically with a very small (and decreasing) penetration rate determined by concrete permeability. However, if a (vertical) flexural crack is present, the acidic water will penetrate along this crack and the degradation will occur also within the crack, particularly at the crack tip. Then, as the crack tip is degraded, it will lose bearing capacity and the crack will propagate, creating new surface area that is exposed to the acidic water. This chemo-mechanical mechanism is recursively repeated driving the propagation of a crack that under purely mechanical loading would be stable.

In order to mimic this mechanism in a very simplified manner, a two-dimensional (plane stress) beam in a three-point bending loading scheme is considered as depicted in Fig. 11. The beam is discretised with 660 quadrangular quadratic continuum elements and a line of 30 quadratic zero-thickness interface elements is inserted along the central

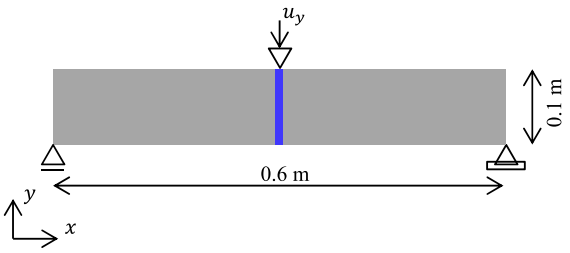

Fig. 11. Application example: subcritical cracking due to chemical degradation. Model geometry and boundary conditions.

cross-section to represent the potential crack. Moreover, it is assumed that the value of the chemical degradation rate will be the same for all the interface integration points along the vertical crack, but that degradation at a given point will only start after that point has started cracking ($W^{cr} > 0$). The degradation rate value has been adopted as $d\eta/dt = 1$.

Continuum elements are assumed linear elastic, with Young modulus $E = 25000$ MPa and Poisson's coefficient $\nu = 0.20$. Interface elements are equipped with the constitutive law presented in Section 2, with the same parameters as for constitutive verification tests (Section 3), with the exception of the initial tensile strength value which is assumed $\chi_o = 2.7$ MPa.

The beam is initially loaded with a negative vertical displacement which is applied at midspan, on the upper face of the beam. The value of the prescribed vertical displacement is adjusted so that the first interface element from the lower face of the beam reaches the onset of cracking. Then, this initial vertical displacement value is kept constant until the end of the test.

The deformed mesh and the normal stresses along the interface elements for this initial condition are indicated with time $t = 0$ in Fig. 12. The high value of normal compression stress at the top of the stress profile are attributed to the effect of stress concentration around the nodes with the imposed vertical displacement. This is the initial state for the chemical degradation process, which starts from the bottom interface element and progresses upwards, leading at each interface point involved, to the contraction of the cracking surface and the consequent reduction of the tensile strength (χ). The tensile strength reduction at the first (bottom) interface element leads to stress redistribution involving the increase of tensile stresses values along all other interface elements above it. Eventually, this stress redistribution causes the cracking of the second interface element, triggering its chemical degradation. As time goes by, this process causes the upward propagation of the initial crack, as it is shown in Fig. 12.

It has to emphasised that the very substantial crack propagation (from the onset of cracking at the bottom face to more than 90% of the beam cross-section), as well as the corresponding stress redistribution observed in Fig. 12, occur for a constant value of prescribed displacement, and are caused exclusively by the chemical degradation process and its interaction (coupling) with the mechanical behaviour of the beam.

4.2. Cracking of chemically degraded mortar specimen

The second example consists of the chemo-mechanical test carried out by Le Bellégo et al. (2000). The purpose of the experimental program was to assess the flexural behaviour of mortar beams that have been previously exposed to an ammonium nitrate solution. Exposed to this corrosive solution, portlandite in the hydrated cement paste is dissolved leading to a calcium leaching process. This process is manifested as a sharp degradation front advancing from the exposed sample surface towards its interior.

The tested specimens were $40 \times 80 \times 320$ mm^3 prismatic mortar beams. The beams were immersed in the ammonium nitrate solution during different periods of time of 28, 56 and 98 days. Only the two lateral faces of the beams were exposed to leaching in order to have two unidirectional leaching fronts through the thickness of the beam. The other faces were covered with an impervious silicon resin (Fig. 13a). The study of a cross section of a leached beam, showed two degraded zones surrounding a sound zone in the centre (Fig. 13b). The depth of the degradation fronts (x_d in Fig. 13b) was measured via phenolphthalein staining and electronic microprobes, after the flexural tests. Based on this measurement, the leaching rate $L_r = 2x_d/B$ is defined as the fraction of the cross section of the beam that has been leached. For 28, 56 and 98 days in the corrosive solution, the leaching rates were 45%, 63.5%, and 84%, respectively.

After the chemical degradation stage, three-point bending tests with notch opening control were performed. For this purpose, a 8 mm deep and 3 mm thick notch was sawed from the bottom face centre of each specimen. A second extensometer followed the vertical displacement ('deflection') of a point at mid-height of the central cross-section of the beam. The results obtained by Le Bellégo et al. (2000) are reproduced in Figs. 14 and 15 in terms of load versus Crack Mouth Opening Displacement (CMOD) and load versus deflection, respectively.

The full geometry and boundary conditions of the test are depicted in Fig. 16a, although due to symmetry the geometry and boundary conditions considered for the analysis correspond to 1/4 of the beam as depicted in Fig. 16b. The body of the specimen is discretised in 3D with 6560 hexahedric linear continuum elements. Along the symmetry plane xy, 160 quadrangular interface elements are inserted to represent the crack propagation. The total number of nodes is 8127. As boundary conditions, the vertical (y-direction) displacement of the nodes along the lateral beam support is restricted, as well as the x-displacements of the nodes on the symmetry plane yz and the z-displacements of the nodes on the symmetry plane xy. The bending load is applied as an imposed vertical displacement of the nodes along the central support in the negative y-direction. This vertical displacement is applied in variable increments governed by an automatic incrementation algorithm. The simulations performed have required between 124 and 131 increments. Convergence in each increment is obtained typically after 3 to 7 iterations.

The continuum elements are assumed to be linear elastic and the interface elements are equipped with the constitutive law developed in this paper. Since the penetration depth of the degradation front at the time of the test is known for each test, the model domain is divided in sound and degraded zones accordingly. Because calcium leaching modifies the cement paste micro-structure, increasing its porosity, the elastic modulus of the degraded material is lower than the that of the sound one (Gérard, 1996). Based on data provided by Le Bellégo et al. (2000) and Le Bellégo et al. (2003), the elastic modulus of the sound and degraded zones are 38.5 GPa and 10.0 GPa, respectively, and the Poisson's modulus is 0.24 in both cases. For the interface elements in the sound zone, the following parameters have been fitted by backward analysis of the bending tests on non-degraded specimens ($L_r = 0\%$): $\chi_o = 4.5$ MPa, $G^I_{Fo} = 3.5 \times 10^{-5}$ MN/m, and $\alpha^{\omega}_{\chi} = -1$. The parameters $c_o = 7$ MPa and $\tan\phi_o = 0.88$ have been arbitrarily chosen with the only precaution of satisfying Eq. (2) and obtaining a small curvature of the tip of the hyperbola in order to facilitate the convergence under tensile loading. Note that because the interface elements are placed on the symmetry plane xy, only normal stress can be developed. The normal and shear stiffness (penalty) coefficients are $K^o_N = K^o_L = 1 \times 10^8$ MPa/m. The chemical degradation variable and the parameters related to the chemical degradation were obtained by simultaneous fitting of the bending test results corresponding to the three degradation rates, namely: $\eta = 0.5$, $G^I_{Fr} = 0.1 \times G^I_{Fo}$, and $= \alpha^{\eta}_{\chi} = \alpha^{\eta}_{G} = -1$. The remaining parameters of the interface constitutive law are irrelevant for this example.

The adoption of an homogeneous value of the degradation variable for all the degraded zone irrespectively of the exposure time is of course a simplification forced by the absence of experimental data on the

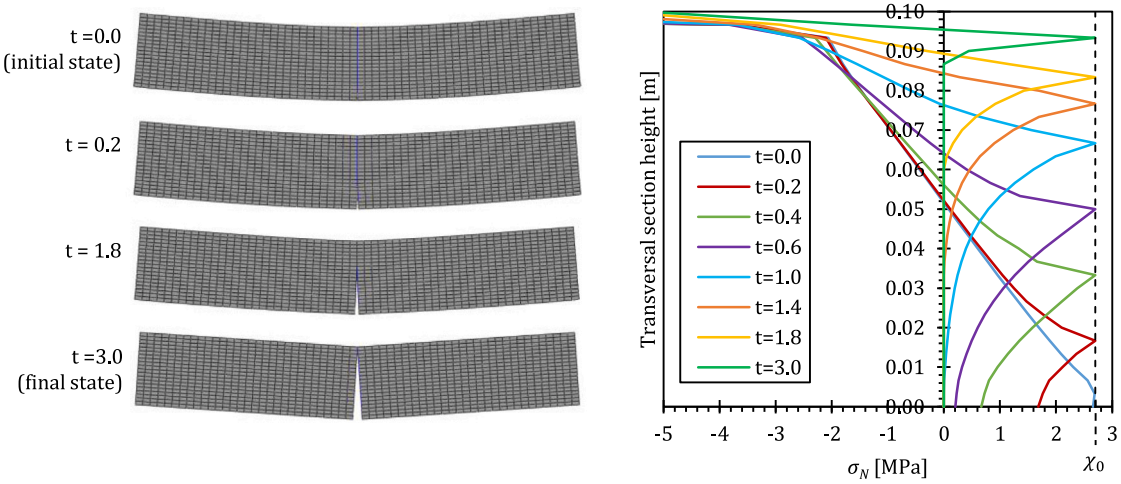

Fig. 12. Application example: subcritical cracking due to chemical degradation. Left: deformed FE mesh (×200) at different times. Right: time evolution of the normal stress profile of the central section of beam as the fracture progresses due to chemical degradation.

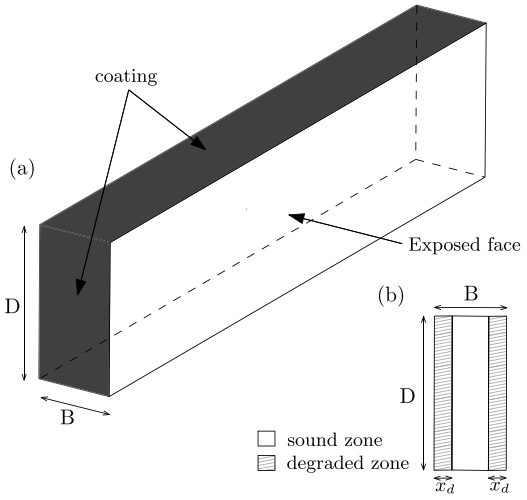

Fig. 13. Application example: Cracking of a chemically degraded mortar specimen. Specimens tested by Le Bellégo et al. (2000). (a) Specimen geometry and lateral coating. (b) Cross section of a leached beam.

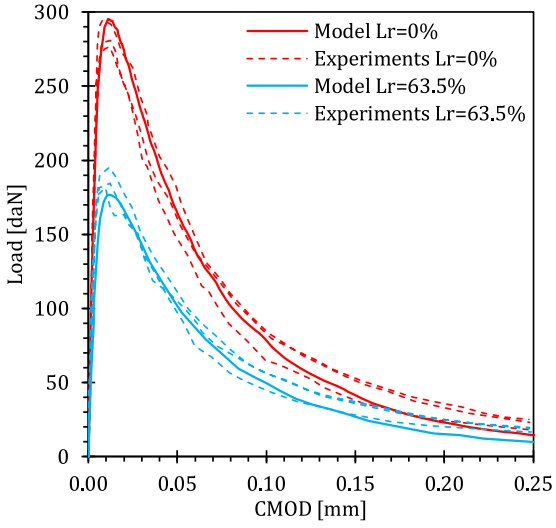

Fig. 14. Application example: Cracking of a chemically degraded mortar specimen. Load–CMOD curves from experimental and numerical three-point bending tests of sound ($L_r = 0\%$) and degraded specimens ($L_r = 63.5\%$). Experimental curves digitised from Le Bellégo et al. (2000). Each dashed line corresponds to a single experiment.

actual degradation profiles. A basis for this simplification may have some grounding in the work by Carde et al. (1996) who observed that, in cement paste samples exposed to similar conditions, the average calcium concentration in the degraded zone remains constant regardless the depth of the degradation front. This was observed as long as some unaltered material remained in the sample core. Therefore, if one assumes a linear relationship between calcium concentration and mechanical degradation, the average mechanical strength of the degraded zone should also constant regardless the depth of the degradation front.

In Figs. 14 and 15, the load–displacement curves obtained with the numerical simulations are plotted together with the experimental results. It can be observed in both figures that the model fits well the experimental curves in terms of the initial (uncracked) stiffness, the peak load and softening evolution, for the four degradation rates considered ($L_r = 0, 45, 63.5$ and 84%). Fig. 17 shows contour plots of the tensile stress and the internal history variable over the fracture plane obtained from the cases with $L_r = 0$ and $L_r = 63.5\%$ and for three different levels of CMOD. The black zones in the contour plots correspond to the compressed zones of the cross section ($\sigma_N < 0$ and $\omega = 0$), which are out of the colour scale. In the non-degraded specimen, the values of σ_N and ω remain uniform in the horizontal direction. In contrast, the degraded specimen shows a clearly different response for the non-degraded zones and the degraded zones, with lower σ_N and ω values in the latter. Note that in both specimens the non-degraded material shows similar values of σ_N and ω for a given value of CMOD.

5. Concluding remarks

A new constitutive law for zero-thickness interface elements has been presented which is capable of reproducing fracturing processes in cement-based materials exposed to chemical degradation.

The main characteristics of the new law are:

- A previous constitutive law formulated in the elasto-plasticity framework and which uses concepts and parameters from the theory of nonlinear fracture mechanics has been taken as a starting point. As a fracture criterion, a hyperbolic surface is used, expressed in terms of three parameters: the tensile strength (vertex of the hyperbola), the apparent cohesion and the angle of internal friction (parameters of the asymptote).

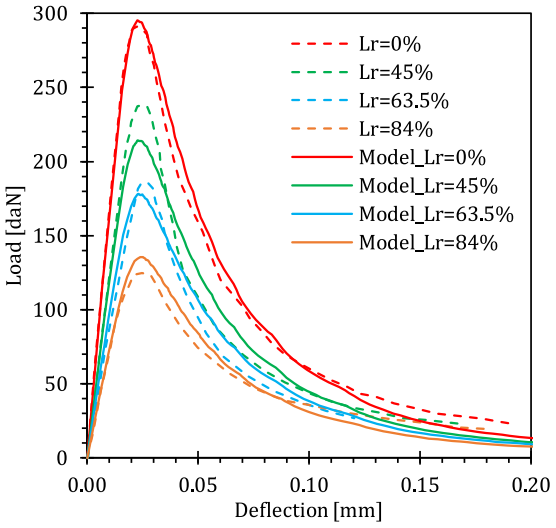

Fig. 15. Application example: Cracking of a chemically degraded mortar specimen. Load–deflection curves from experimental and numerical three-point bending tests of specimens with different leaching rates (L_r). Experimental curves digitised from Le Bellégo et al. (2000). Each dashed line represents the average of a minimum of 3 experiments.

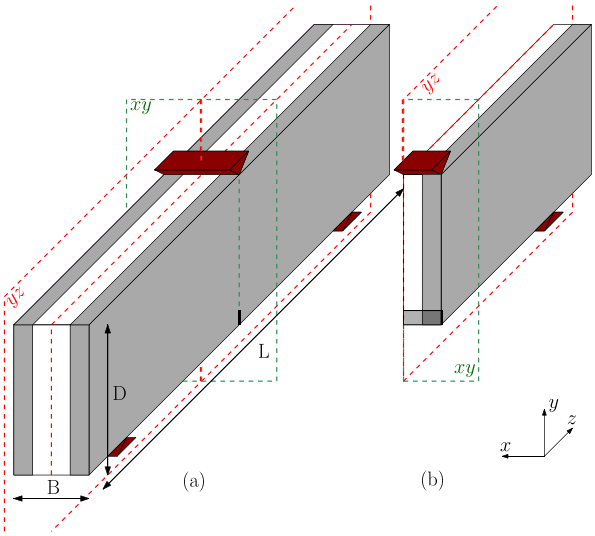

Fig. 16. Application example: Cracking of a chemically degraded mortar specimen. Geometry and boundary conditions of: (a) Real specimen, and (b) Model. Note: B = 40 mm, D = 80 mm, L = 320 mm, Span = 240 mm.

- The evolution of the cracking surface parameters are governed by two history variables, one internal, which represents the degradation associated with fracture processes and the other external, which represents the degree of chemical degradation.
- As in the original model, two energy parameters are used to control the evolution of the cracking surface due to fracture processes: (i) the classical fracture energy in Mode I and (ii) the fracture energy in Mode IIa, corresponding to fracturing due to shear under high compression and without dilation. However, in the new law these parameters are not constant any more, but they progressively decrease with the advance of the chemical degradation of the material.

The performance of the proposed law has been firstly verified at the constitutive level, for pure tensile and mixed shear–compression loading, combined with different sequences of chemical degradation. Subsequently, an academic example has been presented that simulates the propagation of a small, initially stable, bending crack in a beam due to chemical degradation at the tip of the crack. The model has been able to reproduce the subcritical propagation of the crack as the tip is chemically degraded, mechanical strength is lost and the stresses in the beam are redistributed. This simple example illustrates that the interaction (coupling) between chemical degradation and mechanical behaviour including cracking and fracture, may lead to dramatic magnification of effects such as the cracking of the whole cross section caused by a chemical degradation process that, if considered only in the bulk material (continuum) would barely have any noticeable effect on the structural behaviour. Finally, the ability of the new constitutive law to reproduce experimental results has been tested by simulating the three-point bending tests carried out by Le Bellégo et al. (2000) on mortar beams previously exposed to an aggressive solution for different time periods. The results, compared in terms of load–displacement diagrams for different degradation levels, show that the model adequately fits the experimental curves, capturing the decrease of the initial stiffness, peak load and fracturing work as the time of previous exposure to chemical degradation increases.

It should be noticed that experimental evidence on mechanical properties of chemically degraded mortar or concrete is scarce, and, in most cases, reduced to basic uniaxial compression tests or indirect tensile (Brazilian) tests. In this context, the authors were compelled to make some assumptions regarding the behaviour of the degraded material that may lack of direct experimental contrasting for the time being. These assumptions may need to be revised when relevant experimental data becomes available.

The present paper is focused on the interface model formulation itself, assuming that the evolution of the chemical degradation parameter is a known input. Making simplifying assumptions or taking advantage of experimental measurements, it has been possible to assume the values of the chemical degradation parameter and develop the examples presented in the paper. But, it is obvious that in the general case a separate calculation of the chemical diffusion–reaction problem, possibly coupled to the mechanical calculation, should be also needed. Current efforts of the authors are precisely oriented to coupling this constitutive law with a previously developed diffusion–reaction model (Liaudat et al., 2018). This may be done in two different ways: (i) by first obtaining the chemical degradation variable at the integration points of the continuum elements, and then interpolating it to the integration points of the interface elements, or (ii) by assigning a fictitious initial width of material to the interface elements and directly computing the chemical reactions at the interface integration points. The latter approach would require to use chemo-mechanical interface elements as proposed by the authors in the context of alkali-silica reaction in concrete (Liaudat et al., 2020).

Declaration of competing interest

The authors declare that they have no known competing financial interests or personal relationships that could have appeared to influence the work reported in this paper.

Acknowledgments

This research is supported by grants BIA2016-76543-R from MEC (Madrid), Spain, which includes FEDER, Spain funds, and 2017SGR-1153 from AGAUR (Generalitat de Catalunya, Barcelona), Spain. The first author thanks the scholarship 2017FI-B00559 received from AGAUR (Generalitat de Catalunya, Barcelona), Spain.

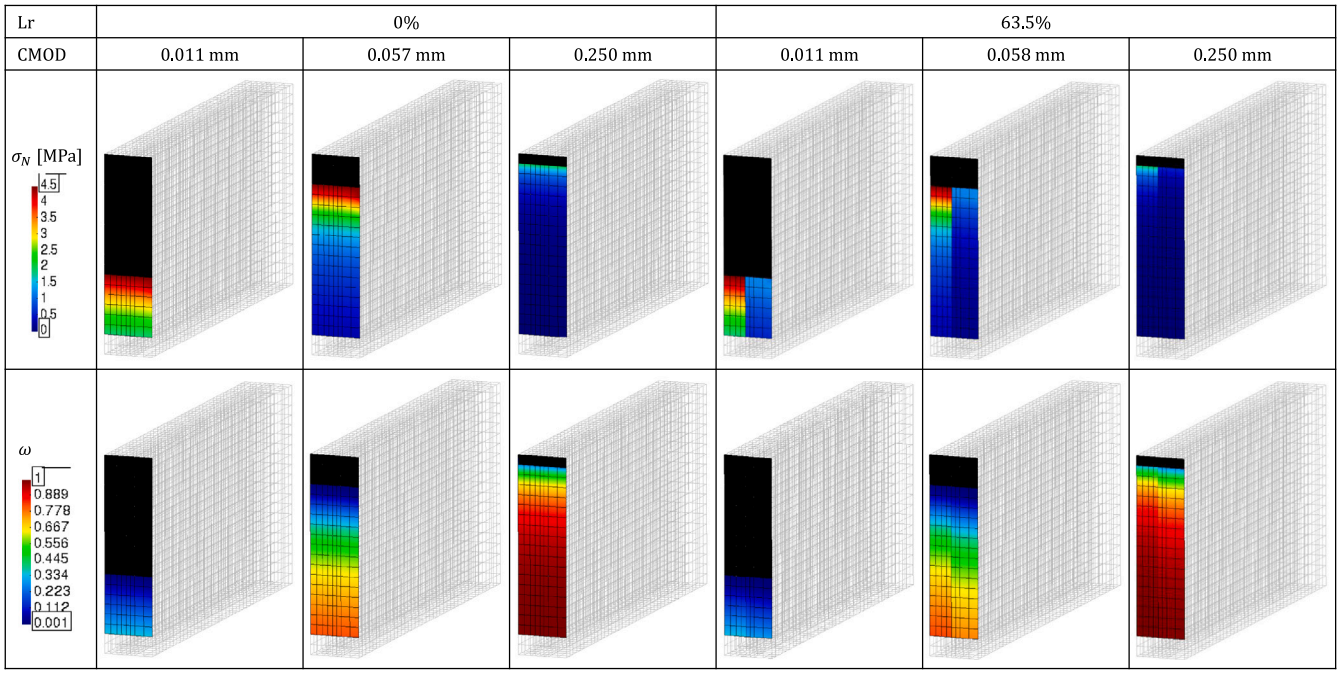

Fig. 17. Application example: Cracking of a chemically degraded mortar specimen. Contour plot of the tensile stress (σ_N) and the internal history variable (ω) over the interface (fracture) plane, for two leaching rates (L_r) and three crack mouth opening displacements (CMOD). Black zones correspond to compressed zones ($\sigma_N < 0$ and $\omega = 0$). (For interpretation of the references to colour in this figure legend, the reader is referred to the web version of this article.)

References

Alfano, G., Crisfield, M.A., 2001. Finite element interface models for the delamination analysis of laminated composites: Mechanical and computational issues. Internat. J. Numer. Methods Engrg. 50 (7), 1701–1736. http://dx.doi.org/10.1002/nme.93.

Alfano, G., Marfia, S., Sacco, E., 2006. A cohesive damage-friction interface model accounting for water pressure on crack propagation. Comput. Methods Appl. Mech. Engrg. 196 (1–3), 192–209. http://dx.doi.org/10.1016/j.cma.2006.03.001.

Atkinson, R., Amadei, B., Saeb, S., Sture, S., 1989. Response of mansonry bed joints in direct shear. J. Struct. Eng. 115 (9), 2276–2296. http://dx.doi.org/10.1061/(ASCE)0733-9445(1989)115:9(2276).

Barenblatt, G., 1962. The mathematical theory of equilibrium cracks in brittle fracture. Adv. Appl. Mech. 7, 55–129. http://dx.doi.org/10.1016/S0065-2156(08)70121-2.

Caballero, A., 2005. 3D Meso-Mechanical Numerical Analysis of Concrete Fracture Using Interface Elements (Ph.D. thesis). Universitat Politècnica de Catalunya.

Caballero, A., Carol, I., López, C.M., 2007. 3D meso-mechanical analysis of concrete specimens under biaxial loading. Fatigue Fract. Eng. Mater. Struct. 30 (9), 877–886. http://dx.doi.org/10.1111/j.1460-2695.2007.01161.x.

Caballero, A., López, C.M., Carol, I., 2006. 3D meso-structural analysis of concrete specimens under uniaxial tension. Comput. Methods Appl. Mech. Engrg. 195 (52), 7182–7195. http://dx.doi.org/10.1016/j.cma.2005.05.052.

Caballero, A., Willam, K.J., Carol, I., 2008. Consistent tangent formulation for 3D interface modeling of cracking/fracture in quasi-brittle materials. Comput. Methods Appl. Mech. Engrg. 197 (33–40), 2804–2822. http://dx.doi.org/10.1016/j.cma.2008.01.011.

Caggiano, A., Etse, G., 2015. Coupled thermo-mechanical interface model for concrete failure analysis under high temperature. Comput. Methods Appl. Mech. Engrg. 289, 498–516. http://dx.doi.org/10.1016/j.cma.2015.02.016.

Camacho, G.T., Ortiz, M., 1996. Computational modelling of impact damage in brittle materials. Int. J. Solids Struct. 33 (20–22), 2899–2938. http://dx.doi.org/10.1016/0020-7683(95)00255-3.

Carde, C., François, R., Torrenti, J.-M., 1996. Leaching of both calcium hydroxide and C-S-H from cement paste: Modeling the mechanical behavior. Cem. Concr. Res. 26 (8), 1257–1268.

Carey, J.W., Wigand, M., Chipera, S.J., WoldeGabriel, G., Pawar, R., Lichtner, P.C., Wehner, S.C., Raines, M.A., Guthrie, G.D., 2007. Analysis and performance of oil well cement with 30 years of CO2 exposure from the SACROC unit, West Texas, USA. Int. J. Greenhouse Gas Control 1 (1), 75–85. http://dx.doi.org/10.1016/S1750-5836(06)00004-1.

Carol, I., López, C.M., Roa, O., 2001. Micromechanical analysis of quasi brittle materials using fracture based interface elements. Internat. J. Numer. Methods Engrg. 52, 193–215. http://dx.doi.org/10.1002/nme.277.

Carol, I., Prat, P.C., López, C.M., 1997. Normal/shear cracking model: Application to discrete crack analysis. J. Eng. Mech. 123 (8), 765–773. http://dx.doi.org/10.1061/(ASCE)0733-9399(1997)123:8(765).

Carrier, B., Granet, S., 2012. Numerical modeling of hydraulic fracture problem in permeable medium using cohesive zone model. Eng. Fract. Mech. 79, 312–328. http://dx.doi.org/10.1016/j.engfracmech.2011.11.012.

Cerfontaine, B., Dieudonné, A.C., Radu, J.P., Collin, F., Charlier, R., 2015. 3D zero-thickness coupled interface finite element: Formulation and application. Comput. Geotech. 69, 124–140. http://dx.doi.org/10.1016/j.compgeo.2015.04.016.

Chen, J., Crisfield, M., Kinloch, A.J., Busso, E.P., Matthews, F.L., Qiu, Y., 1999. Predicting progressive delamination of composite material specimens via interface elements. Mech. Compos. Mater. Struct. 6 (4), 301–317. http://dx.doi.org/10.1080/107594199305476.

D'Aguiar, S.C., Modaressi-Farahmand-Razavi, A., dos Santos, J.A., Lopez-Caballero, F., 2011. Elastoplastic constitutive modelling of soil-structure interfaces under monotonic and cyclic loading. Comput. Geotech. 38 (4), 430–447. http://dx.doi.org/10.1016/j.compgeo.2011.02.006.

Desai, C., Zamman, M., Lightner, J., Siriwardane, H., 1984. Thin-layer element for interfaces and joints. J. Numer. Anal. Methods Geomech. 8 (1), 19–43. http://dx.doi.org/10.1002/nag.1610080103.

Dugdale, D.S., 1960. Yielding of steel sheets containing slits. J. Mech. Phys. Solids 8 (2), 100–104. http://dx.doi.org/10.1016/0022-5096(60)90013-2.

Duguid, A., Scherer, G.W., 2010. Degradation of oilwell cement due to exposure to carbonated brine. Int. J. Greenhouse Gas Control 4 (3), 546–560. http://dx.doi.org/10.1016/j.ijggc.2009.11.001.

Etse, G., Caggiano, A., Vrech, S., 2012. Multiscale failure analysis of fiber reinforced concrete based on a discrete crack model. Int. J. Fract. 178 (1–2), 131–146. http://dx.doi.org/10.1007/s10704-012-9733-z.

Garolera, D., Carol, I., Papanastasiou, P., 2019. Micromechanical analysis of sand production. Int. J. Numer. Anal. Methods Geomech. 43 (6), 1207–1229. http://dx.doi.org/10.1002/nag.2892.

Gasda, S., Bachu, S., Celia, M., 2004. The potential for CO2 leakage from storage sites in geological media: analysis of well distribution in mature sedimentary basins. Environ. Geol. 46 (6–7), 707–720. http://dx.doi.org/10.1007/s00254-004-1073-5.

Gens, A., Carol, I., Alonso, E.E., 1988. An interface element formulation for the analysis of soil-reinforcement interaction. Comput. Geotech. 7, 133–151. http://dx.doi.org/10.1016/0266-352X(89)90011-6.

Gens, A., Carol, I., Alonso, E.E., 1995. Rock joints: FEM implementation and applications. In: Selvadurai, A.P.S., Boulon, M.J. (Eds.), Mechanics of Geomaterials Interfaces. Elsevier, The Netherlands, pp. 395–420.

Gérard, B., 1996. Contribution of the Mechanical, Chemical, and Transport Couplings in the Long-Term Behavior of Radioactive Waste Respository Structures (in French) (Ph.D. thesis). Université Laval, Québec, Canada / École Normale Supérieure de Cachan, France.

Ghaboussi, J., Wilson, E., Isenberg, J., 1973. Finite element for rock joints and interfaces. J. Soil Mech. Found. Div. 99, 833–848.

Goodman, R., Taylor, R., Brekke, T., 1968. A model for the mechanics of jointed rock. J. Soil Mech. Found. Div. 94 (3), 637–659.

Gui, Y.L., Hu, W., Zhao, Z.Y., Zhu, X., 2018. Numerical modelling of a field soil desiccation test using a cohesive fracture model with Voronoi tessellations. Acta Geotech. 13 (1), 87–102. http://dx.doi.org/10.1007/s11440-017-0558-9.

Hillerborg, A., Modéer, M., Petersson, P.E., 1976. Analysis of crack formation and crack growth in concrete by means of fracture mechanics and finite elements. Cem. Concr. Res. 6 (6), 773–781. http://dx.doi.org/10.1016/0008-8846(76)90007-7.

Idiart, A.E., López, C.M., Carol, I., 2011a. Chemo-mechanical analysis of concrete cracking and degradation due to external sulfate attack: A meso-scale model. Cem. Concr. Compos. 33 (3), 411–423. http://dx.doi.org/10.1016/j.cemconcomp.2010.12.001.

Idiart, A.E., López, C.M., Carol, I., 2011b. Modeling of drying shrinkage of concrete specimens at the meso-level. Mater. Struct. 44 (2), 415–435. http://dx.doi.org/10.1617/s11527-010-9636-2.

IPCC, 2005. In: Metz, B., Davidson, O., de Coninck, H.C., Loos, M., Meyer, L.A. (Eds.), IPCC Special Report on Carbon Dioxide Capture and Storage. Prepared By Working Group III of the Intergovernmental Panel on Climate Change. Cambridge University Press, Cambridge, United Kingdom and New York, NY, USA, p. 442.

Jacobsen, J.S., Poulsen, P.N., Olesen, J.F., Krabbenhoft, K., 2013. Constitutive mixed mode model for cracks in concrete. Eng. Fract. Mech. 99, 30–47. http://dx.doi.org/10.1016/j.engfracmech.2013.01.004.

Jefferson, A.D., 2002. Tripartite cohesive crack model. J. Eng. Mech. 128 (6), 644–653. http://dx.doi.org/10.1061/(asce)0733-9399(2002)128:6(644).

Koutromanos, I., Shing, P.B., 2012. Cohesive crack model to simulate cyclic response of concrete and masonry structures. ACI Struct. J. 109 (3), 349–355.

Kutchko, B.G., Strazisar, B.R., Dzombak, D.a., Lowry, G.V., Thauiow, N., 2007. Degradation of well cement by CO2 under geologic sequestration conditions. Environ. Sci. Technol. 41 (13), 4787–4792. http://dx.doi.org/10.1021/es062828c.

Kutchko, B.G., Strazisar, B., Lowry, G., Dzombak, D., Thaulow, N., 2008. Rate of CO2 attack on hydrated class H well cement under geologic sequestration conditions. Environ. Sci. Technol. 42 (16), 6237–6242. http://dx.doi.org/10.1021/es800049r.

Le Bellégo, C., Gérard, B., Pijaudier-Cabot, G., 2000. Chemo-mechanical effects in mortar beams subjected to water hydrolisis. J. Eng. Mech. 126 (3), 266–272. http://dx.doi.org/10.1061/(ASCE)0733-9399(2000)126:3(266).

Le Bellégo, C., Pijaudier-Cabot, G., Gérard, B., Dubé, J.F., Molez, L., 2003. Coupled mechanical and chemical damage in calcium leached cementitious structures. J. Eng. Mech. 129 (3), 333–341. http://dx.doi.org/10.1061/(ASCE)0733-9399(2003)129:3(333).

Li, Y., Deng, J.G., Liu, W., Feng, Y., 2017. Modeling hydraulic fracture propagation using cohesive zone model equipped with frictional contact capability. Comput. Geotech. 91, 58–70. http://dx.doi.org/10.1016/j.compgeo.2017.07.001.

Liaudat, J., Carol, I., López, C.M., 2020. Model for alkali-silica reaction expansions in concrete using zero-thickness chemo-mechanical interface elements. Int. J. Solids Struct. 207, 145–177. http://dx.doi.org/10.1016/j.ijsolstr.2020.09.019.

Liaudat, J., Martínez, A., López, C.M., Carol, I., 2018. Modelling acid attack of oilwell cement exposed to carbonated brine. Int. J. Greenhouse Gas Control 68C, 191–202. http://dx.doi.org/10.1016/j.ijggc.2017.11.015.

López, C.M., 1999. Análisis microestructural de la fractura del hormigón utilizando elementos finitos tipo junta. Aplicación a diferentes hormigones (Ph.D. thesis). Universitat Politècnica de Catalunya.

López, C.M., Carol, I., Aguado, A., 2008a. Meso-structural study of concrete fracture using interface elements. I: numerical model and tensile behavior. Mater. Struct. 41 (3), 583–599. http://dx.doi.org/10.1617/s11527-007-9314-1.

López, C.M., Carol, I., Aguado, A., 2008b. Meso-structural study of concrete fracture using interface elements. II: compression, biaxial and Brazilian test. Mater. Struct. 41 (3), 601–620. http://dx.doi.org/10.1617/s11527-007-9312-3.

Lotfi, H.R., Shing, P.B., 1994. Interface model applied to fracture of masonry structures. J. Struct. Eng. 120 (1), 63–80. http://dx.doi.org/10.1061/(ASCE)0733-9445(1994)120:1(63).

Lourenço, P., 1996. Computational Strategies for Masonry Structures (Ph.D. thesis). Delft University of Technology.

Manzoli, O., Sánchez, M., Maedo, M., Hajjat, J., Guimarães, L.J., 2018. An orthotropic interface damage model for simulating drying processes in soils. Acta Geotech. 13 (5), 1171–1186. http://dx.doi.org/10.1007/s11440-017-0608-3.

Marques, J., 1984. Stress computation in elastoplasticity. Eng. Comput. 1 (1), 42–51. http://dx.doi.org/10.1108/eb023559.

Nguyen, V.P., Lian, H., Rabczuk, T., Bordas, S., 2017. Modelling hydraulic fractures in porous media using flow cohesive interface elements. Eng. Geol. 225 (November 2016), 68–82. http://dx.doi.org/10.1016/j.enggeo.2017.04.010.

Oliveira, D.V., Lourenço, P.B., 2004. Implementation and validation of a constitutive model for the cyclic behaviour of interface elements. Comput. Struct. 82 (17–19), 1451–1461. http://dx.doi.org/10.1016/j.compstruc.2004.03.041.

Pande, G.N., Beer, G.G., Williams, J.R., 1990. Numerical Methods in Rock Mechanics. John Wiley & Sons.

Parrinello, F., Marannano, G., Borino, G., 2016. A thermodynamically consistent cohesive-frictional interface model for mixed mode delamination. Eng. Fract. Mech. 153, 61–79. http://dx.doi.org/10.1016/j.engfracmech.2015.12.001.

Pérez, A., Rodriguez, M., López, C.M., Carol, I., 2013. 3D meso-mechanical analysis of cracking and spalling of concrete subject to high temperatures. In: Oñate, E., Owen, D., Peric, D., Suárez, B. (Eds.), Computational Plasticity XII - Fundamentals and Applications. International Center for Numerical Methods in Engineering (CIMNE), Barcelona, Spain, pp. 1015–1025, URL http://congress.cimne.com/complas2013/proceedings/full/p722.pdf.

Pérez-Foguet, A., Rodríguez-Ferran, A., Huerta, A., 2001. Consistent tangent matrices for substepping schemes. Comput. Methods Appl. Mech. Engrg. 190 (35–36), 4627–4647. http://dx.doi.org/10.1016/S0045-7825(00)00336-4.

Plesha, M.E., 1987. Constitutive model for rock discontinuities with dilatancy and surface degradation. Int. J. Numer. Anal. Methods Geomech. 11 (4), 345–362. http://dx.doi.org/10.1002/nag.1610110404.

Pouya, A., Vo, T.D., Hemmati, S., Tang, A.M., 2019. Modeling soil desiccation cracking by analytical and numerical approaches. Int. J. Numer. Anal. Methods Geomech. 43 (3), 738–763. http://dx.doi.org/10.1002/nag.2887.

Puntel, E., Bolzon, G., Saouma, V.E., 2006. Fracture mechanics based model for joints under cyclic loading. J. Eng. Mech. 132 (11), 1151–1159. http://dx.doi.org/10.1061/(ASCE)0733-9399(2006)132.

Rimmelé, G., Barlet-Gouédard, V., Porcherie, O., Goffé, B., Brunet, F., 2008. Heterogeneous porosity distribution in portland cement exposed to CO2-rich fluids. Cem. Concr. Res. 38 (8–9), 1038–1048. http://dx.doi.org/10.1016/j.cemconres.2008.03.022.

Rots, J., 1988. ComputationaL Modelling of Concrete Fracture (Ph.D. thesis). Delft University of Technology, The Netherlands.

Rueda-Cordero, J.A., Mejia-Sanchez, E.C., Roehl, D., 2019. Hydromechanical modeling of unrestricted crack propagation in fractured formations using intrinsic cohesive zone model. Eng. Fract. Mech. 221 (August), 106655. http://dx.doi.org/10.1016/j.engfracmech.2019.106655.

Segura, J.M., Carol, I., 2004. On zero-thickness interface elements for diffusion problems. Int. J. Numer. Anal. Methods Geomech. 28 (9), 947–962. http://dx.doi.org/10.1002/nag.358.

Spada, A., Giambanco, G., Rizzo, P., 2009. Damage and plasticity at the interfaces in composite materials and structures. Comput. Methods Appl. Mech. Engrg. 198 (49–52), 3884–3901. http://dx.doi.org/10.1016/j.cma.2009.08.024.

Stankowski, T., Runesson, K., Sture, S., 1993a. Fracture and slip of interfaces in cementitious composites. I: Characteristics. 119, (2), pp. 292–314. http://dx.doi.org/10.1061/(ASCE)0733-9399(1993)119:2(292),

Stankowski, T., Runesson, K., Sture, S., 1993b. Fracture and slip of interfaces in cementitious composites. II: Implementation. J. Eng. Mech. 119 (2), 315–327. http://dx.doi.org/10.1061/(ASCE)0733-9399(1993)119:2(315).

Wang, J., Jivkov, A.P., Li, Q.M., Engelberg, D.L., 2020. Experimental and numerical investigation of mortar and ITZ parameters in meso-scale models of concrete. Theor. Appl. Fract. Mech. 109 (July), http://dx.doi.org/10.1016/j.tafmec.2020.102722.

Willam, K., Bićanić, S., 1984. Constitutive and computational aspects of strain softening and localization in solids. In: Willam, K. (Ed.), ASME-WAM'84 Symposium on Constitutive Equations. ASME Press, New Orleans (USA), pp. 233–252.

Willam, K., Rhee, I., Shing, B., 2004. Interface damage model for thermomechanical degradation of heterogeneous materials. Comput. Methods Appl. Mech. Engrg. 193 (30–32), 3327–3350. http://dx.doi.org/10.1016/j.cma.2003.09.020.